Kinetic pathways to hidden quantum states via laser-engineered topological defects

Zhihui Zhou,[1,2,*] Hengxin Tan,[3,*] Chenhang Xu,[4,5] Qing Xu,[1,2] Chao Xu,[6] Shaozheng Wang,[3,7] Jing Xu,[1,2] Yang Lv,[1,2] Li Chen,[1,2] Yicheng Li,[2,3] Dupeng Zhang,[2,8] Xiao Zou,[1,2] Pengfei Zhu,[1,8] Tao Jiang,[1,2] Jun Li,[9] Shuaishuai Sun,[9] Anshul Kogar,[10] Alfred Zong,[4,5] Shengwei Jiang,[3,7] Ye Zhu,[6] Dao Xiang,[1,2,8,†] and Xinshu Zhang[2,3,‡]

[1]*Key Laboratory for Laser Plasmas (Ministry of Education), School of Physics and Astronomy, Shanghai Jiao Tong University, Shanghai 200240, China*
[2]*Zhangjiang Institute for Advanced Study, Shanghai Jiao Tong University, Shanghai 201210, China*
[3]*Key Laboratory of Artificial Structures and Quantum Control (Ministry of Education), School of Physics and Astronomy, Shanghai Jiao Tong University, Shanghai 200240, China*
[4]*Departments of Physics and of Applied Physics, Stanford University, Stanford, California 94305, U.S.A.*
[5]*Stanford Institute for Materials and Energy Sciences, SLAC National Accelerator Laboratory, Menlo Park, California 94025, U.S.A.*
[6]*Department of Applied Physics, Research Institute for Smart Energy, The Hong Kong Polytechnic University, Hung Hom, Kowloon, Hong Kong, China*
[7]*State Key Laboratory of Micro-nano Engineering Science, Tsung-Dao Lee Institute, Shanghai Jiao Tong University, Shanghai, 201210, China*
[8]*State key Laboratory of Dark Matter Physics, Tsung-Dao Lee Institute and New Cornerstone Science Laboratory, Shanghai Jiao Tong University, Shanghai 201210, China*
[9]*Beijing National Laboratory for Condensed Matter Physics and Institute of Physics, Chinese Academy of Sciences, Beijing 100190, China*
[10]*Department of Physics and Astronomy, University of California Los Angeles, Los Angeles, CA, USA*

(Dated: June 2, 2026)

Contents

SUPPLEMENTARY NOTE 1:IDENTIFICATION OF SINGLE-DOMAIN ANTIFERROELECTRIC REGIONS

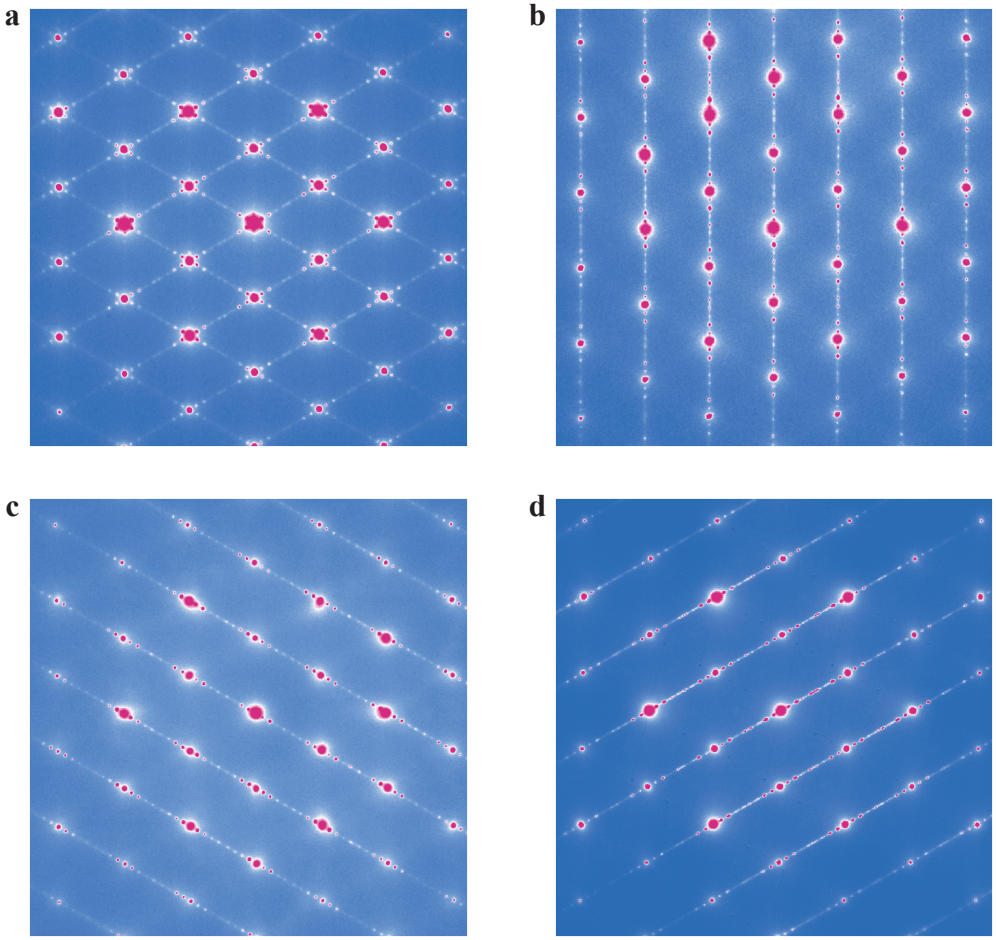

FIG. S1: **Identification of single-domain antiferroelectric regions by UEM.** a, Electron diffraction pattern showing the coexistence of AFE superlattice reflections from two 120° domain orientations. b–d, Representative diffraction patterns acquired from regions containing single AFE domains with distinct superlattice orientations.

The antiferroelectric (AFE) phase of In_2Se_3 exhibits three energetically equivalent domains related by 120° rotational symmetry. In diffraction measurements, superlattice reflections originating from multiple domains are frequently observed, as shown in Fig. S1a. Owing to the high spatial resolution of ultrafast electron microscopy (UEM), diffraction patterns can be acquired from localized regions with dimensions comparable to individual single domains. This capability enables the isolation and characterization of single-domain regions, where only one set of AFE superlattice reflections is observed, as demonstrated in Fig. S1b–d for the three distinct domain orientations. These measurements allow the ultrafast structural dynamics of individual AFE domains to be selectively investigated without contributions from overlapping domains.

SUPPLEMENTARY NOTE 2:ESTIMATED TRANSIENT LATTICE TEMPERATURE FOLLOWING PHOTOEXCITATION

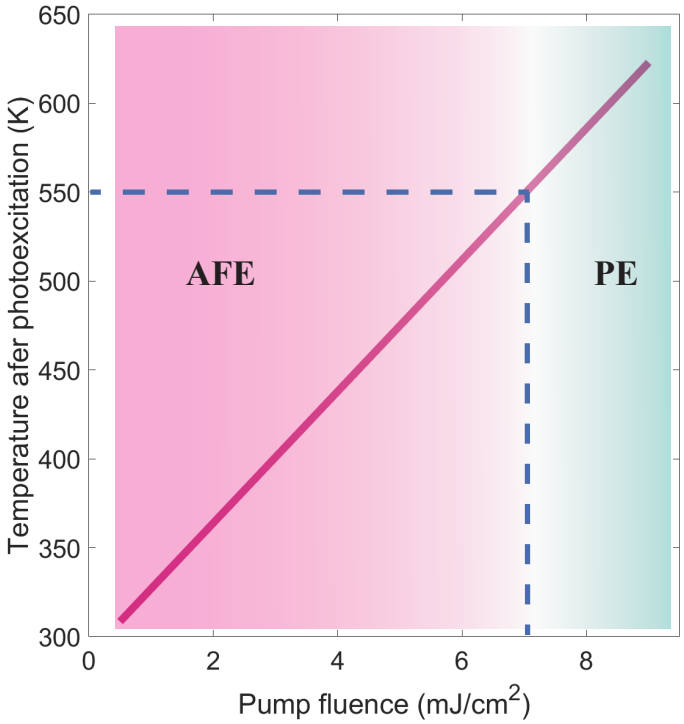

FIG. S2: **Estimated transient lattice temperature of 2H-In_2Se_3 following photoexcitation.** Estimated temperature increase ΔT of the In_2Se_3 sample as a function of pump fluence under 400/520 nm excitation. The transient lattice temperature was estimated according to the absorbed energy density. The dashed horizontal line indicates the approximate AFE to PE transition temperature ($\sim$ 550 K). The estimated transient temperature reaches the phase transition regime at a fluence of approximately 7 mJ/cm^2.

To estimate the transient lattice temperature of In_2Se_3 following ultrafast photoexcitation, we evaluated the absorbed energy density using a simplified optical absorption model [1,2,3]. The absorbed energy density F_{abs} is expressed as

$$F_{abs} = \frac{(1-R)[1-exp(-d/\delta)]F}{d} \tag{S1}$$

where R is the reflectivity, d is the sample thickness, δ is the optical penetration depth, and F is the incident pump fluence.

For the present calculation, we adopted $R = 0.22$, estimated from the optical response of the sample under visible-light excitation [4]. The optical penetration depth was taken as $\delta \approx 100$ nm [4]. The sample thickness was estimated to be $d \approx 50$ nm from TEM measurements. The transient temperature increase was then estimated according to

$$\Delta T = \frac{F_{abs}}{\rho C_p} \tag{S2}$$

where ρ and C_p denote the mass density and specific heat capacity, respectively. We used $\rho = 5.46$ g/cm^3 and $C_p = 0.3$ J/g K. The calculated transient temperature as a function of pump fluence is shown in Fig. S2. The estimated lattice temperature reaches approximately 550 K at a fluence near 7 mJ/cm^2, corresponding to the reported AFE to PE phase transition for In_2Se_3 [5].

SUPPLEMENTARY NOTE 3:ABSENCE OF APPRECIABLE BRAGG PEAK BROADENING

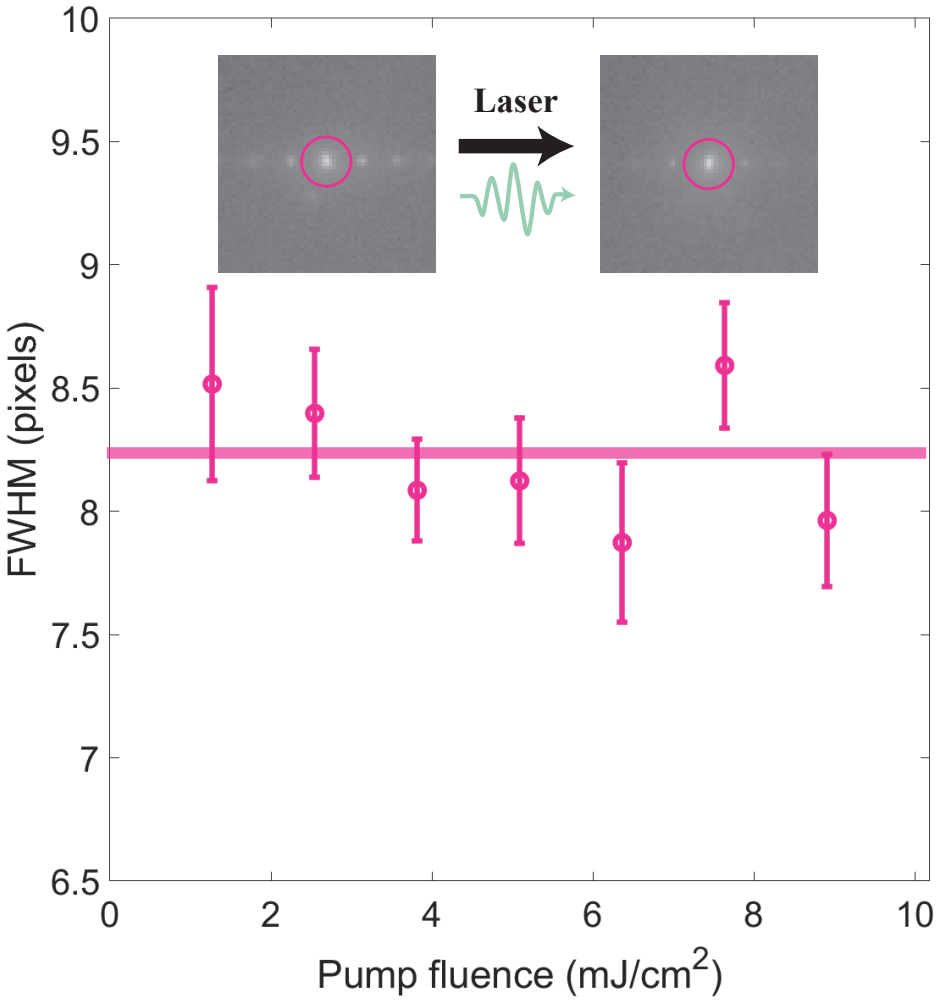

FIG. S3: **FWHM of the Bragg peaks as a function of pump fluence.** In contrast to the pronounced broadening of the superlattice reflections, the Bragg peaks remain nearly resolution-limited over the entire fluence range. The error bars represent standard deviation. Insets show enlarged diffraction patterns near a representative Bragg reflection before and after photoexcitation above the threshold fluence. The absence of appreciable Bragg peak broadening rules out significant lattice disorder or point-defect generation induced by the optical pulse.

To further clarify the microscopic origin of the metastable AFE* state and rule out conventional point defects, we analyzed the linewidth of the fundamental Bragg peaks. A key observation is that the linewidth broadening induced by optical excitation occurs only in the superlattice reflections, while the fundamental Bragg peaks remain nearly unchanged. As shown in Fig. S3, the full width at half maximum (FWHM) of the Bragg peaks exhibits negligible fluence dependence even above the threshold fluence required for AFE* formation. Since conventional point defects or strong lattice disorder would broaden both Bragg and superlattice reflections simultaneously, the absence of appreciable Bragg peak broadening combined with notable superlattice peaks broadening provides robust evidence that the optical pulse specifically generates topological defects rather than generic lattice damage such as point defects.

SUPPLEMENTARY NOTE 4:THERMAL ERASURE AND RECOVERY OF THE ANTIFERROELECTRIC SUPERSTRUCTURE

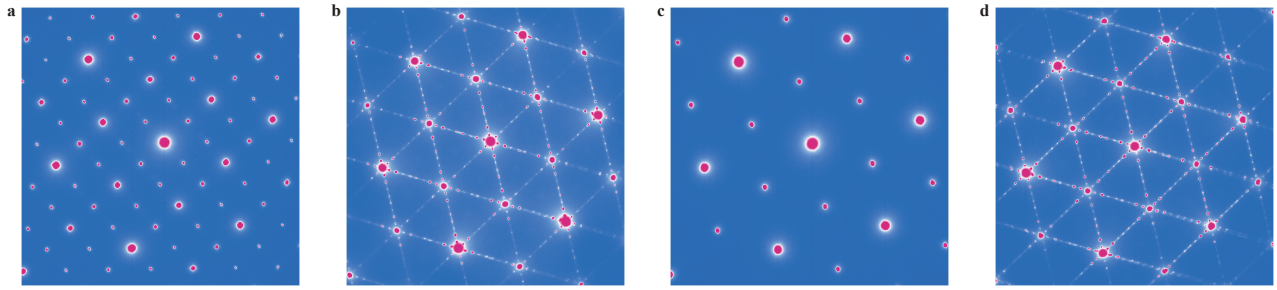

FIG. S4: **Thermal erasure and recovery of the antiferroelectric superstructure.** a, Electron diffraction pattern of the CDW phase at 100 K, characterized by the emergence of the $2 \times \sqrt{3}$ superstructure reflections. b, Diffraction pattern measured at room temperature after warming from the CDW phase. The CDW reflections disappear and the diffraction pattern reverts to the AFE* state, exhibiting the characteristic 1/8 superlattice reflections. c, Diffraction pattern measured after heating the sample to 550 K. The 1/8 superlattice reflections disappear completely, indicating the transition to the high-symmetry PE phase. d, Upon cooling the sample from 550 K to room temperature, the system transitions to the AFE phase. Further cooling to 100 K maintains the AFE phase without the reappearance of CDW reflections, confirming that thermal cycling through the PE phase effectively erases topological defects and suppresses CDW formation upon subsequent cooling.

To investigate the stability and reversibility of the defect-engineered phase pathway, we performed systematic temperature dependent diffraction measurements from 100 K to 550 K. After the hidden CDW phase is formed at low temperature (Fig. S4a), warming the sample to room temperature causes the CDW reflections to disappear while the characteristic 1/8 antiferroelectric superlattice reflections emerge (Fig. S4b). Upon subsequent cooling, the CDW phase reappears, demonstrating a reversible switching cycle between the AFE* and CDW states.

In contrast, a qualitatively different behavior is observed when the sample is heated above 550 K. At this temperature, all 1/8 superlattice reflections vanish completely (Fig. S4c), signifying a transition into the high-symmetry paraelectric (PE) phase [5]. After cooling back to room temperature, the system recovers the pristine AFE phase. Further cooling no longer produces the hidden CDW state, and only the equilibrium AFE superstructure is observed (Fig. S4d).

These results demonstrate that the photo-induced AFE* state retains a topological memory that survives over repetitive thermal cycling between room temperature and the low temperature. This memory enables the reversible AFE*–CDW switching observed in the main text. However, heating into the paraelectric phase completely removes the topological defects responsible for this behavior, thereby restoring the original equilibrium pathway.

SUPPLEMENTARY NOTE 5:REAL-SPACE EVIDENCE OF TOPOLOGICAL DEFECTS

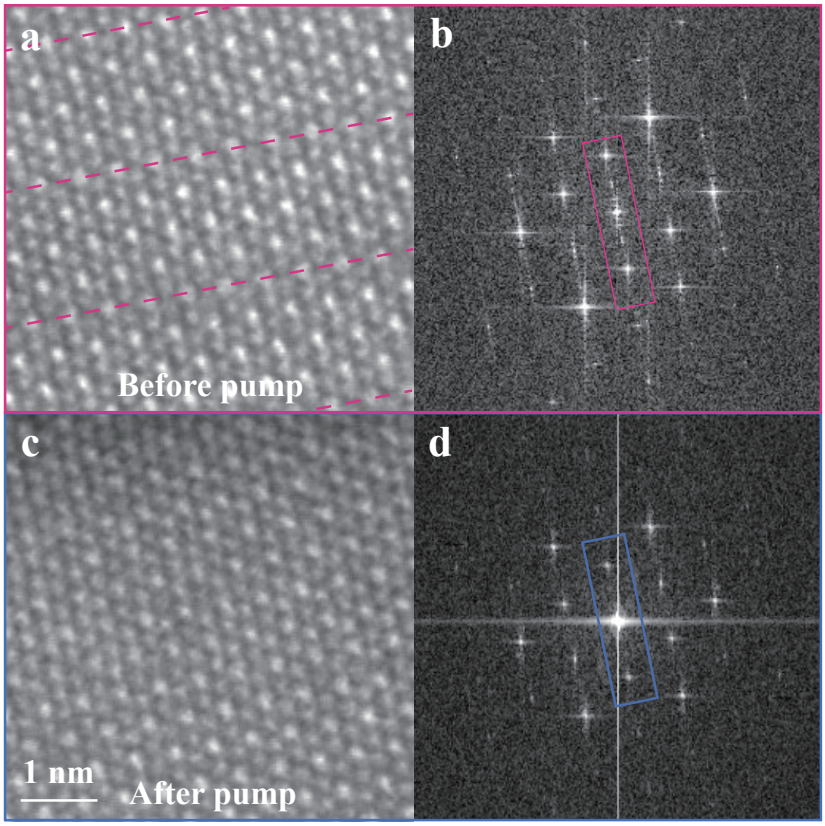

FIG. S5: **Atomic-resolution HAADF-STEM images and corresponding fast Fourier transform (FFT) patterns before and after photoexcitation.** a,b, Before pumping, the AFE nanostripe order is well defined in real space, and clear superlattice reflections are observed in the FFT pattern. The red dashed lines indicate the periodicity of the superlattice modulation, while the red solid box marks the reciprocal space associated with the AFE order parameter. c,d, After photoexcitation, the striped modulation becomes fragmented into nanodomains and the corresponding superlattice reflections are strongly suppressed, indicating a local reduction of the AFE order parameter.

Direct real-space evidence for the defect-mediated state is provided by aberration-corrected HAADF-STEM imaging. Before photoexcitation, the AFE nanostripe pattern is spatially uniform and produces well-defined superlattice reflections in reciprocal space. After pumping, the striped modulation becomes fragmented into nanoscale domains, accompanied by a substantial suppression of the corresponding fast Fourier transform (FFT) intensity. These observations show that the AFE order parameter becomes locally suppressed in these regions, which are consistent with the formation of topological defects at the junctions of these nanodomains.

SUPPLEMENTARY NOTE 6:DETAILS OF SPATIAL PHASE DISTRIBUTION

To elucidate the microscopic nature of the laser-induced metastable state, we extracted the spatial phase distribution of the AFE modulation from the atomic resolution HAADF-STEM images using a Fourier filtering technique via standard Digital Micrograph routines and custom image processing scripts. The detailed analytical procedure is outlined as follows:

1. Fast Fourier Transform (FFT): First, a two-dimensional FFT is applied to the real-space atomic image (Fig. 3f(i)). This converts the spatial information into momentum space, producing the corresponding diffractogram shown in the inset of Fig. 3f(ii).

2. Reciprocal Space Masking: In the Fourier domain, the primary lattice Bragg peaks and the AFE superlattice reflections are distinctly separated. We isolate the structural modulation by applying a localized mask (indicated by the green circle) strictly around a specific superlattice reflection associated with the AFE order. All other spatial frequencies outside this aperture are filtered out (set to zero) to remove noise and decouple the underlying lattice from the modulation of interest.

3. Inverse Fast Fourier Transform (IFFT): An IFFT is then performed on this isolated frequency region. Because the masking breaks the inversion symmetry of the Fourier spectrum in reciprocal space, the resulting real-space signal is a complex-valued function, which can be expressed as:

$$f(r) = A(r)exp[i\phi] \tag{S3}$$

where r is the spatial coordinate, A represents the local amplitude, and ϕ is the local geometric phase of the AFE modulation.

4. Phase Mapping: By taking the argument of this complex function, we extract the two-dimensional spatial phase map ϕ. Before photoexcitation, this phase distribution is highly uniform, representing perfectly aligned and well-ordered AFE stripes. In contrast, after pumping, the extracted spatial phase map (Fig. 3f(iv)) exhibits abrupt discontinuities and pronounced phase offsets. These localized phase slips and domain walls act as topological defects, offering heterogeneous nucleation sites for subsequent CDW formation.

SUPPLEMENTARY NOTE 7:RAMAN SCATTERING SIGNATURES OF THE HIDDEN QUANTUM STATE

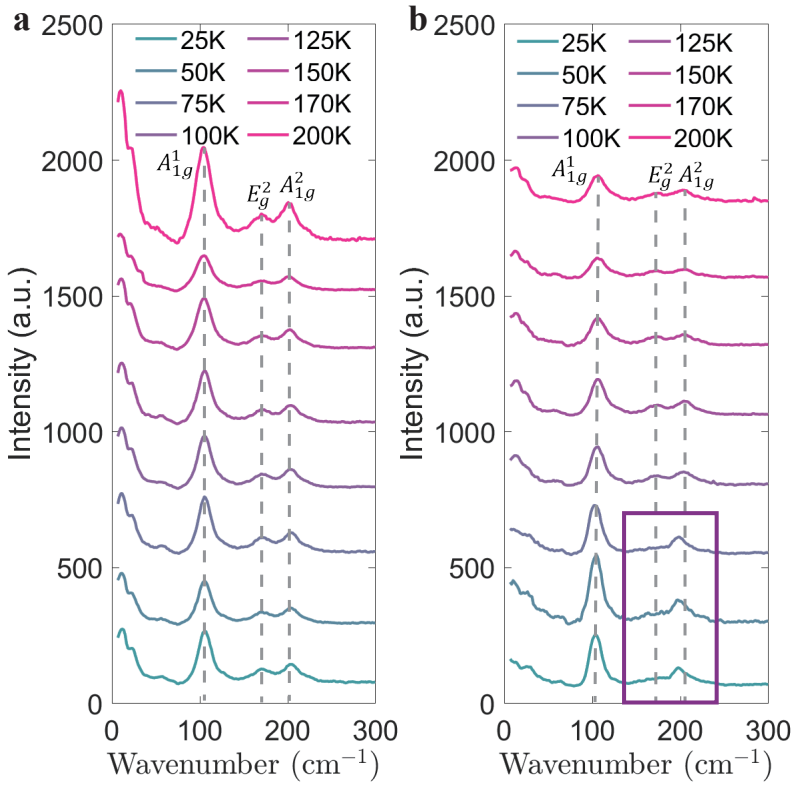

FIG. S6: **Temperature-dependent Raman spectroscopy of the pristine and photoexcited samples.** a, Raman spectra of the pristine sample measured upon cooling from 200 K to 25 K. The characteristic phonon modes remain stable across the entire temperature range, indicating the preservation of the AFE phase. Gray dashed lines are provided as guides to the eye for the specific peak positions. b, Raman spectra of the photoexcited sample over the same temperature range. At room temperature, the spectrum is identical to that of the pristine state, confirming the absence of a direct light-induced phase transition. However, at low temperatures (25 K, 50 K, and 75 K), the E^2_g peak vanishes, and the A^2_{1g} mode clearly shifts to a lower wavenumber (redshift) as marked by the purple box. These distinct spectral changes confirm that the laser-engineered topological defects successfully guide the system into a structurally distinct CDW phase at low temperatures.

To further verify the structural evolution and provide macroscopic spectroscopic evidence for the hidden phase transition, we performed temperature dependent Raman scattering measurements on both the pristine and photoexcited samples. At room temperature, the Raman spectra of both samples are virtually indistinguishable, which confirms that the laser pulse itself does not directly drive a structural phase transition. Instead the ultrafast optical quench generates a high density of topological defects to form the metastable AFE* state, these highly localized defects merely reconfigure the existing displacement pattern without altering the global lattice symmetry. Due to the spectral resolution limits of our optical Raman measurements, no obvious peak broadening are resolved at room temperature.

However, upon thermodynamic cooling, the two samples exhibit divergent trajectories. In the pristine sample (Fig. S6a), the characteristic phonon modes remain robust without any abrupt anomalies from 200 K down to 25 K. This indicates that the pristine sample remains deeply trapped in the kinetically stable AFE phase.

In stark contrast, the photoexcited sample (Fig. S6b) undergoes a distinct structural transformation at low temperatures. Below 100 K (specifically observed at 75 K, 50 K, and 25 K), the E^2_g characteristic peak completely disappears. Additionally, the A^2_{1g} mode exhibits a pronounced anomalous redshift. These distinct phonon anomalies corroborate a symmetry breaking and phase transition to the CDW state.

SUPPLEMENTARY NOTE 8:DIVERGENCE OF THE STRUCTURAL RELAXATION TIME

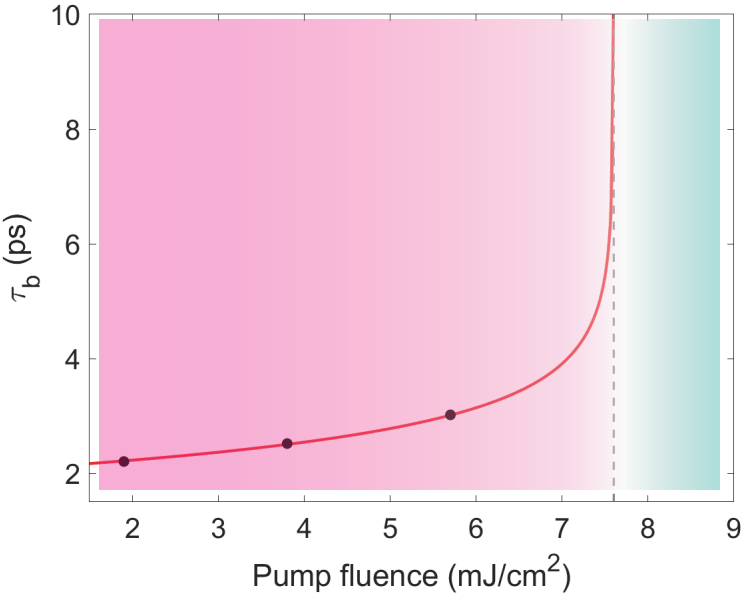

FIG. S7: **Critical slowing down and divergence of the structural relaxation time.** Pump fluence dependence of the extracted relaxation time constant τ_b for the AFE superlattice peaks. The gray dashed line (fluence = 7.6 mJ/cm^2) indicates the singularity of the fitting function (location of the asymptote). Below 6 mJ/cm^2, the system exhibits rapid structural recovery. As the fluence approaches the critical threshold of 7.6 mJ/cm^2, τ_b exhibits a dramatic divergence, signifying the transition from a transient structural perturbation to the formation of a topologically protected metastable state characterized by robust phase slips and domain walls. The red curves are the fit with Eq. S5.

To quantitatively map the threshold behavior of the light-induced metastable state, we extracted the relaxation time constant τ_b of the AFE superlattice reflections across a wide range of pump fluences. The time-dependent normalized intensity profiles, as shown in Fig. 3(d) of the main text, were fitted using a double exponential recovery model:

$$\Delta I = A\exp(-t/\tau_a) - B\exp(-t/\tau_b) + C \tag{S4}$$

where τ_a and τ_b denote the time constants for intensity decay and recovery, respectively. The extracted recovery time constant τ_b was fitted using a critical power-law divergence model:

$$\tau_b = a + \frac{b}{(F_c - F)^c} \tag{S5}$$

The fitting as a function of pump fluence is summarized in Fig. S7. Two distinct kinetic regimes are clearly resolved:

Perturbative Regime (Fluence $\leq$ 6 mJ/cm^2): At lower excitation densities, the optical pulse merely acts as a mild perturbation to the pristine AFE order. The atomic displacements rapidly relax back to their equilibrium positions, characterized by a fast and relatively stable recovery time constant on the order of a few picoseconds. As the fluence increases towards 6 mJ/cm^2, τ_b exhibits only a marginal and gradual increase, consistent with standard thermalization and lattice cooling processes.

Topological defect generation regime (Fluence $>$ 7.6 mJ/cm^2): As the pump fluence exceeds 6 mJ/cm^2 and approaches a critical threshold, the relaxation dynamics undergo a fundamental change. The recovery time becomes progressively longer and eventually diverges completely at 7.6 mJ/cm^2. This macroscopic divergence indicates that the system is no longer relaxing into the initial pristine AFE phase. During the subsequent rapid structural recovery, spontaneous symmetry breaking occurs locally, generating a dense network of misaligned stripes and phase slips via the Kibble-Zurek mechanism. The topological protection of these newly formed defects intrinsically traps the material in a robust metastable state, preventing the re-establishment of the long-range AFE correlation and thereby causing the observed divergence in the structural recovery time.

SUPPLEMENTARY NOTE 9:DECOUPLED AMPLITUDE AND PHASE DYNAMICS IN ULTRAFAST ELECTRON DIFFRACTION

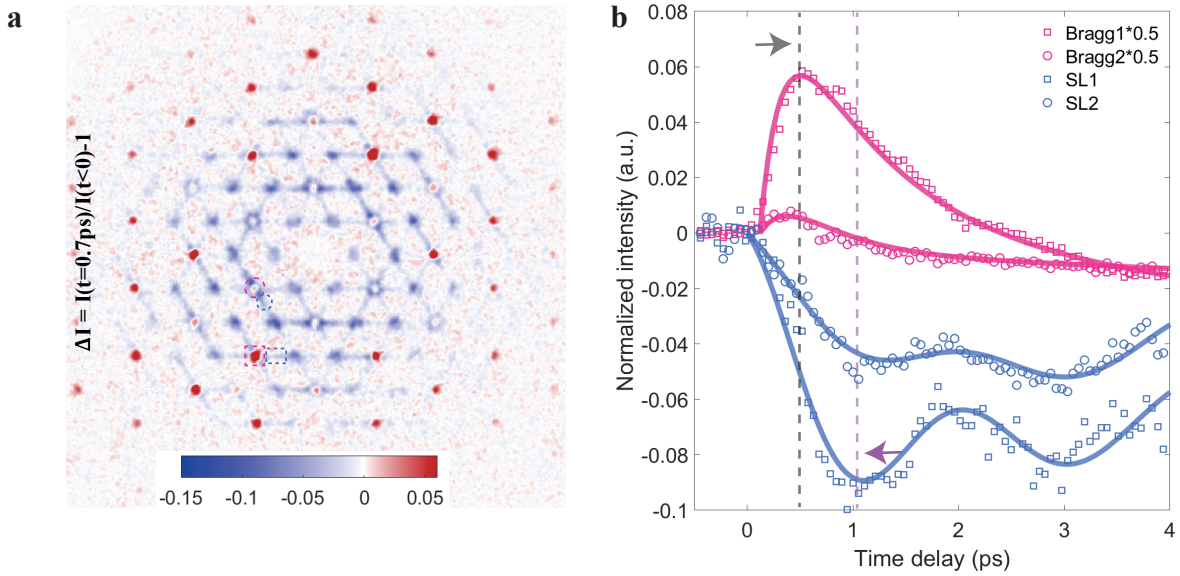

FIG. S8: **Transient suppression and recovery dynamics of the structural order.** a, Differential ultrafast electron diffraction pattern measured at a pump–probe delay of 0.7 ps. Red and blue correspond to intensity increase and decrease, respectively. The elongated blue features around the superlattice reflections indicate a transient suppression of the superlattice order following photoexcitation. b, Temporal evolution of the diffraction intensity from the Bragg peaks (red) and superlattice peaks (blue). The Bragg peak intensity begins to recover at approximately 0.5 ps and nearly reaches equilibrium within 3 ps, whereas the superlattice recovery starts at 1 ps and remains unrecovered after 4 ps. These distinct timescales are attributed to the amplitude and phase dynamics of the AFE order, respectively.

Additional support for the formation of a topologically defective state is obtained from time-resolved ultrafast electron diffraction (UED) measurements. The differential diffraction pattern at a pump–probe delay of 0.7 ps reveals elongated intensity suppression exclusively around the superlattice reflections, demonstrating the transient melting of the long-range superstructure. Furthermore, the corresponding temporal evolution shows markedly different recovery dynamics for the Bragg and superlattice peaks. The Bragg peaks recover rapidly within several picoseconds, reflecting the fast recovery of the lattice distortion amplitude.

In contrast, the superlattice peaks exhibit a delayed and substantially slower recovery. This indicates that while the local amplitude is restored quickly, the phase coherence of the ordered state remains disrupted over much longer timescales. Such decoupled amplitude and phase dynamics are classic, definitive signatures of photo-induced topological defects in symmetry-broken phases [6, 7, 8].

SUPPLEMENTARY NOTE 10:LATTICE STRUCTURES AND ATOMIC DISTORTION PATTERNS OF THE QUANTUM PHASES FOR DFT

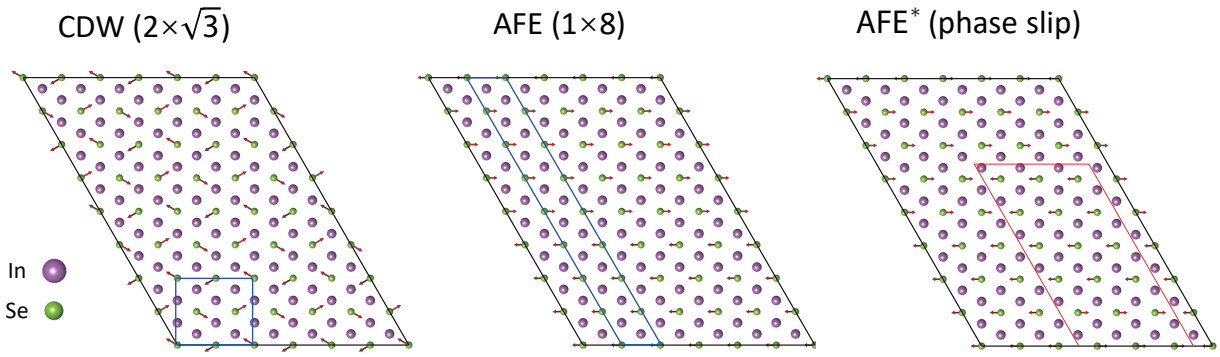

FIG. S9: Lattice structures and atomic distortion patterns used for DFT calculations. Top view of the atomic displacements for the $2 \times \sqrt{3}$ CDW, pristine 1×8 AFE, and the metastable AFE* phase hosting topological defects (specifically, misaligned stripe domains). All structures are visualized within a 6×8 supercell. Red arrows indicate the in-plane displacement vectors of the inner Se atoms. The outermost Se atoms in all structures are omitted for clarity. Blue box in left panel indicates the local unit of the $2 \times \sqrt{3}$ CDW. Blue quadrilateral in middle panel delineates the primitive unit cells for 1×8 AFE. Red lines highlight the emergent domain walls in the AFE* structure.

To establish a comprehensive microscopic understanding of the phase competition and the crucial role of topological defects in In_2Se_3, we visualized the lattice structures of the relevant quantum phases based on our density functional theory (DFT) calculations. Fig. S9 illustrates the the atomic distortion patterns for the hidden ground state, the pristine equilibrium state, and the AFE* state. The hidden CDW phase is characterized by a $2 \times \sqrt{3}$ periodicity, whereas the pristine equilibrium AFE phase exhibits a long-range, well-ordered 1×8 superstructural modulation driven by the antiparallel displacements of the inner Selenium (Se) atoms. To theoretically model the AFE* with topological defects, we explicitly constructed misaligned AFE stripe domains within the structural lattice. As highlighted in Fig. S9, these misaligned regions form distinct domain walls that locally disrupt the pristine AFE order parameter. As discussed in the main text (Fig. 4), the explicit inclusion of these localized structural imperfections in our DFT framework confirms that such topological defects raise the local energy of the AFE phase, thereby efficiently reducing the kinetic barrier required to transition into the global energy minimum of the CDW phase.

* These authors contributed equally.
† Electronic address: dxiang@sjtu.edu.cn
‡ Electronic address: zxinshu@sjtu.edu.cn

[1] J.Li et al. Femtosecond Electron Diffraction Reveals Local Disorder and Local Anharmonicity in Thermoelectric SnSe. *Adv. Mater.* **36**, 2313742 (2024).
[2] Krishnamoorthy A. et al. Optical Control of Non-Equilibrium Phonon Dynamics. *Nano Lett.* **19**, 4981 (2019).
[3] J. Yang et al. Tracking Ultrafast Ion Diffusion Dynamics in AgCrSe2 Superionic Conductor. *Phys. Rev. X* **16**, 021024 (2026).
[4] C. Julien et al. Electrical and optical properties of In2Se3 thin films. *Thin Solid Films* **137**, 27-37 (1986).
[5] Changxi Zheng et al. Room temperature in-plane ferroelectricity in van der Waals In2Se3. *Sci. Adv.* **4**, eaar7720 (2018).
[6] Zong, A. et al. Evidence for topological defects in a photoinduced phase transition. *Nat. Phys.* **15**, 27–31 (2019).
[7] Kogar, A. et al. Light-induced charge density wave in LaTe3. *Nat. Phys.* **16**, 159–163 (2020).
[8] Cheng, Y. et al. Ultrafast formation of topological defects in a two-dimensional charge density wave. *Nat. Phys.* **20**, 54–60 (2024).